Građevinski materijali i konstrukcije
Building Materials and Structures
journal homepage: www.buildingmaterialsstructures.com

https://doi.org/10.5937/GRMK2500011B UDK: 624.073.012.45

Original scientific paper

Influence of concrete damaged plasticity model parameters on punching shear behavior of reinforced concrete flat slabs

Smilja Bursać[1)], Martina Vojnić Purčar[1)], Ljiljana Kozarić[1)], Mila Svilar[*1)]

[1)] *University of Novi Sad, Faculty of Civil Engineering Subotica, Kozaračka 2a, 24000 Subotica, Serbia*

Article history

Received: 26 September 2025
Received in revised form: 07 November 2025
Accepted: 17 November 2025
Available online: 26 November 2025

Keywords

Concrete Damaged Plasticity model,
Punching Shear,
RC Slabs

ABSTRACT

This study examines the influence of Concrete Damaged Plasticity (CDP) model parameters on the punching shear behavior of reinforced concrete (RC) flat slabs using non-linear finite element analysis (NLFEA) in Abaqus. The CDP model, known for its ability to simulate the inelastic behavior of concrete under multiaxial stress states, was calibrated based on the author's previously published experimental results. The calibration process involved variation of key CDP parameters and finite element mesh sizes. Following validation on a reference slab, the model was applied to six additional slabs that varied in three primary aspects: presence of openings, loading eccentricity, and cross-sectional dimensions of the supporting column. The findings indicate that variations in CDP parameters have a notable impact on the simulated punching behavior. However, when appropriately defined, the CDP model enables accurate prediction of punching shear capacity, thereby reducing the need for costly and time-consuming experimental testing.

1 Introduction

Flat slabs have become a standard floor system in residential, commercial, and industrial buildings due to their architectural flexibility, rapid construction, reduced story height, and simple integration of services. These benefits, however, comes with certain drawbacks: the slab–column connection is susceptible to punching shear, a brittle and sudden failure mode that can precipitate progressive collapse if not properly controlled [1- 8].

Punching shear develops in the zone of concentrated support reactions, leading to a truncated cone (or pyramid) failure surface around the column footprint as load and rotation increase. Classical formulations based on critical sections and empirical design rules have been progressively refined by mechanical models and the critical shear crack theory (CSCT), which explicitly relates punching capacity to slab rotation and crack kinematics. The governing parameters include slab thickness (effective depth), longitudinal reinforcement ratio and grade, concrete compressive strength, column geometry, and the presence and amount of shear reinforcement [4, 8].

To date, a variety of shear reinforcement solutions have been investigated to enhance punching resistance and ductility, such as headed studs, closed stirrups, multi-leg or truss-shaped stirrups, and spiral systems. Recent research emphasize the role of anchorage and position of reinforcements—especially the interaction with flexural reinforcement—in activation shear reinforcement. Inclined or spiral arrangements of reinforcement often provides favorable performance [7, 9]. Also, studies on fiber-reinforced concrete slabs (with steel or synthetic fibers) show significant improvements in load capacity and energy absorption due to crack bridging and better post-cracking behavior, although model predictions and design codes vary considerably [10].

Material innovations—from ultra-high-performance concrete (UHPC) to sustainable mixes incorporating recycled constituents—exhibit distinct punching behaviors. Reinforced UHPC slabs benefit from higher tensile and compressive strengths, while hybrid eco-mixes can modify toughness and stiffness with mixed effects on ultimate capacity; these observations are relevant to both concentric and non-concentric loading scenarios and to systems with openings [11-12].

In practice, the layout of building services frequently requires openings near columns. Openings reduce the concrete area of the critical punching perimeter and often interrupt flexural reinforcement, thereby increasing local shear stresses and decreasing both strength and deformation capacity. Experimental and numerical studies consistently demonstrate that the reduction depends on opening size, shape, number, and—critically—location relative to the column and load path [6, 13-14]. Strengthening with externally bonded systems (e.g., CFRP strips, textile-reinforced mortar, or aluminum sheets) and with embedded systems (e.g., GFRP gratings) can partially or fully recover the loss in punching capacity, but the gain depends on the configuration, anchorage, and stiffness of the strengthening system [13, 15-16].

* Corresponding author:
E-mail address: milasvilar@gmail.com

Loading eccentricity introduces unbalanced moments at slab–column connections, increasing shear on the more heavily loaded side and reducing the effective punching resistance. Even small eccentricities can decrease capacity and change crack patterns, yet current regulations provisions typically treat eccentricity in simplified ways and, in many cases, ignore the interaction with discontinuities such as openings adjacent to column faces [6, 17]. The combined effect of eccentricity and openings remains insufficiently represented in design approaches, despite being common in real buildings.

Synthesis of recent literature indicate a major deficiency: while openings and eccentricity have been studied separately, their combined effect—especially the position of openings relative to the eccentricity side—is underrepresented in design provisions and remains insufficiently quantified. Živković et al. [18] and Bursać et al. [19] report that international design codes generally neglect the opening position with respect to the eccentricity side, despite its significant influence on punching behavior. Moreover, available design provisions may underestimate or overestimate capacity under these combined actions, and recommended strengthening configurations are not yet unified for such cases [6, 9-10, 13].

Combined with experiments, non-linear finite element analysis (NLFEA) has become an important tool for predicting punching shear. The fracture and plasticity models of distributed-cracked concrete, calibrated against reference tests, can reproduce the load-deflection relationship, crack patterns, and failure mode with high accuracy, enabling systematic parametric analysis of geometry, reinforcement, openings, and load eccentricity. However, there are still differences between NLFEA predictions, laboratory tests and simplified formulations in the codes - especially for weakly reinforced or large slabs, as well as in cases where unbalanced moments are combined with discontinuities [6, 8, 13].

Therefore, the main objective of this study is to provide a detailed assessment of how variations in key numerical simulation parameters affect the punching shear behavior of reinforced concrete (RC) slabs. Special attention is given to the punching behavior of flat slabs with openings subjected to eccentric loading. The adopted eccentricity value of 150 mm was introduced to simulate the effect of unbalanced moments that naturally occur in real flat slabs. In actual structures, such moments develop due to the transfer of bending moments between the slab and the column, as well as due to load asymmetry, edge or corner column locations, and the presence of openings near the column. This value was also selected based on literature data [20], as similar eccentricities are commonly analyzed in experimental and numerical studies. The eccentricity was therefore chosen to realistically reproduce the combined bending and punching shear behavior observed in real slab–column connections.

2 Description of the analyzed slabs

This study uses experimental results previously published by the author [19], which were adapted for the validation and calibration of the nonlinear finite element analysis model. A total of seven RC flat slab models were analyzed under loading applied through an interior column. The primary differences among the individual models lie in the presence and position of the opening relative to the load direction, as well as in column geometry. All slabs share identical dimensions, chosen to align with those most commonly adopted in previous experimental research [21-24]. The slab model was developed to represent the region of negative bending moments in the slab surrounding the internal column. The model diameter is typically taken as 0.44L, where L denotes the axial distance between columns. This value corresponds to the point at which the radial bending moment becomes zero along a circular line of diameter 0.44L centered at the point of support. Each slab has a diameter of 1800 mm, a thickness of 120 mm, and an effective depth of 95 mm.

To facilitate easier formwork in experimental setups, the slabs were cast as regular octagons with side lengths of 746 mm, approximating a circular shape. This configuration has been employed in several previous studies [25-28], and research by [29] confirms that slab shape (square or circular) has no significant effect on punching capacity.

The tension zone of each slab was reinforced with 10 mm diameter bars placed in two orthogonal directions at 100 mm spacing, while the compression zone was reinforced with bars of the same diameter at 200 mm spacing. Slabs were intentionally engineered to fail in punching shear, with flexural reinforcement carefully dimensioned to ensure such a failure mode. The reinforcement layout differed between the tension and compression zones—tension reinforcement was provided in accordance with flexural capacity requirements, while compression reinforcement was limited to the minimum amount needed to control shrinkage and temperature effects. Although increasing the amount of compression reinforcement to match that in the tension zone is typically recommended for improved structural behavior under eccentric loading, the configuration used in this study was selected to replicate an unfavorable scenario that could realistically occur in practice. No additional reinforcement was placed around the opening, allowing for an isolated investigation of its influence on the slab's punching behavior. This approach enables a more accurate assessment of potential strengthening needs and realistically simulates the structural response when an opening is introduced into an existing slab system.

The reference model S1, used as a control specimen, contains no opening and is subjected to centrically applied load through a square column with dimensions 150×150 mm. The slab geometry, dimensions, and reinforcement layout—both in plan and in section—are shown in Figure 1. Model S2 differs from the reference model only in the loading condition: while S1 is loaded concentrically, S2 is subjected to eccentric loading, with the load application point offset by 150 mm from the vertical axis of the column. The effect of an opening near the column under concentric loading was examined in model S3, which retains the same square column dimensions (150×150 mm). Eccentrically loaded slabs with openings were analyzed through models S4 and S5. The column geometry remains unchanged, and the eccentricity is set to 150 mm. In S4, the opening is positioned on the side opposite the load direction, while in S5, the opening is located on the same side as the applied load. The influence of column size variation on punching shear capacity in eccentrically loaded slabs with openings adjacent to the column face was investigated using models S6 and S7. For these specimens, the column cross-section was changed to a 300×150 mm rectangle. Both slabs were loaded with a 150 mm eccentricity. In S6, the opening is placed on the side opposite the load, while in S7, it is located on the same side as the applied load. Figure 2 illustrates the slab geometry, boundary conditions, and loading configurations for all analyzed slabs.

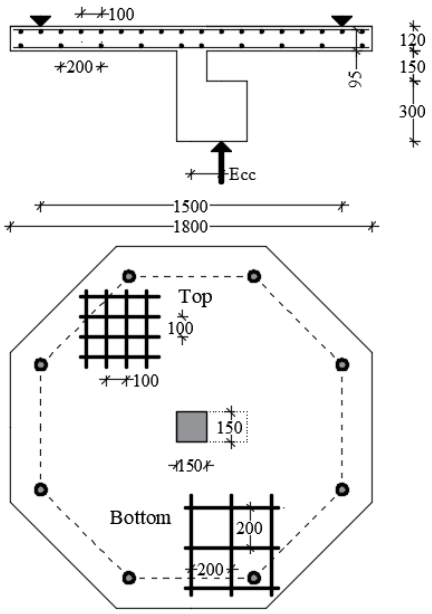

Figure 1. Geometry and reinforcement details of the RC slab

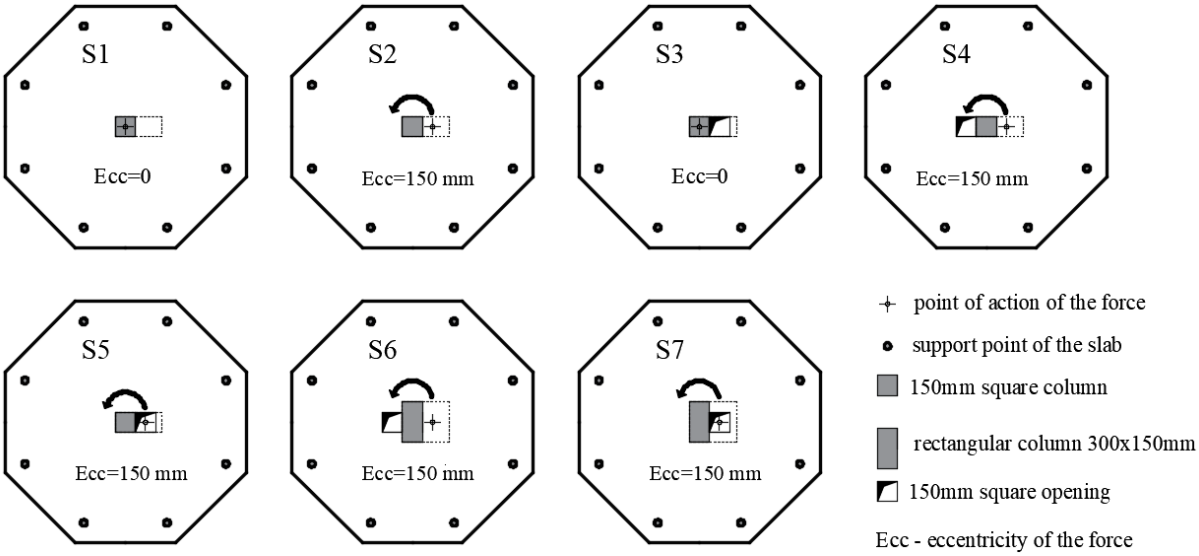

Figure 2. Illustration of slab geometry, boundary conditions, and loading configurations

3 Materials and methods

The non-linear analysis of RC slabs subjected to various loading scenarios and opening positions was conducted using the NLFEA software package Abaqus [30]. The simulation process begins by discretizing the structural system into finite elements defined by multiple nodes. The concrete of both the slab and the column was modeled using C3D8R elements—8-node, reduced integration, 3D solid elements with three translational degrees of freedom per node (in x, y, and z directions). The reinforcement was modeled using T3D2 elements, which are 2-node truss elements defined by cross-sectional area and designed to carry axial tension or compression. Each node in this element also possesses three translational degrees of freedom. These elements are then assembled into a comprehensive numerical model representing the structural behavior under investigation. The solution involves solving a system of algebraic equations that accurately capture the mechanical response of the discretized model.

To simulate the behavior of concrete, the Abaqus software offers several constitutive models. For this study, the concrete damaged plasticity (CDP) model, based on the concept of brittle fracture, was selected to represent the behavior of the slab. A detailed description of the model will be presented in Section 3.2. The column, on the other hand, was modeled as a linearly elastic material. Reinforcing steel was represented using a bilinear stress–strain relationship, assuming elastic–perfectly plastic behavior.

The finite element modeling aimed to replicate the actual behavior of the tested specimens as accurately as possible, allowing for the evaluation of various parameters influencing punching shear capacity—without the need for extensive and costly experimental investigations.

3.1 Characteristics of incorporated materials

The characterization of material properties was carried out prior to the slab testing phase, using specimens sampled during the concreting process. All tests were performed at the Laboratory of the Faculty of Civil Engineering in Subotica. The key mechanical properties — compressive strength (f_c), tensile strength (f_t), and Young's modulus (E_c) — were determined on three standard control cylinders for each test series, and the mean values of the measured results are summarized in Table 1. The splitting tensile strength of the concrete was measured on cylindrical specimens with a diameter of 15 cm and a height of 30 cm. In this test, the tensile strength is determined based on the line load applied along two opposite generatrices of the cylinder ($f_{ct,sp}$). The corresponding axial tensile strength of the concrete was then calculated as $f_t = \alpha_{ct,sp} \cdot f_{ct,sp}$. According to [31], the parameter $\alpha_{ct,sp}$ ranges between 0.67 and 1.1. In this study, the value of this parameter was adopted in accordance with the Eurocode 2 [32] recommendation, where $\alpha_{ct,sp} = 0.9$ is suggested. The modulus of elasticity (E_c) was determined by loading cylindrical specimens (15×30 cm) in compression. The applied compressive force was approximately 30% of the expected failure load of the specimen. During the testing, three fixed frames and seven digital extensometers were used. The accuracy of the deformation measurement device is 1/1000 mm.

The mechanical properties of the reinforcement were obtained through tensile testing conducted on three standard specimens using a universal testing machine. The average values derived from these tests are presented in Table 2.

3.2 CDP model

The CDP model captures both dominant failure mechanisms in concrete: tensile cracking and compressive crushing [33]. A schematic representation of stress–strain responses under uniaxial loading for plasticity-only, damage-only, and combined damage–plasticity models is given in Figure 3. Solid lines denote loading paths, while dashed lines indicate unloading paths. In this context, ε_{el} and ε_{pl} represent elastic and plastic strains, respectively, and E_0 is the initial elastic modulus. As evident from Figure 3, material degradation due to damage reduces stiffness, where the slope of the unloading branch becomes $(1-D)E_0$, with D being the scalar damage parameter. The damage parameter was defined as proposed by [34]: $D = 1 - \sigma/f$, where f represents the compressive or tensile strength of the concrete.

Table 1. Properties of specimens

Slab	Opening [mm]	Eccentricity [mm]	Column [mm]	f_c [MPa]	f_t [MPa]	E_c [GPa]
S1	-	-	150x150	38.73	3.09	30.99
S2	-	150	150x150	41.39	3.21	32.08
S3	150x150	-	150x150	41.39	3.21	32.08
S4	150x150	150	150x150	38.73	3.09	30.99
S5	150x150	150	150x150	38.73	3.09	30.99
S6	150x150	150	300x150	41.39	3.21	32.08
S7	150x150	150	300x150	38.73	3.09	30.99

Table 2. Mechanical properties of reinforcement

Yield strength of flexural reinforcement	f_y [MPa]	595
Ultimate stress	f_u [MPa]	674
Steel strain	ε_y [‰]	2.87
Modulus of elasticity of reinforcement	E_c [GPa]	207

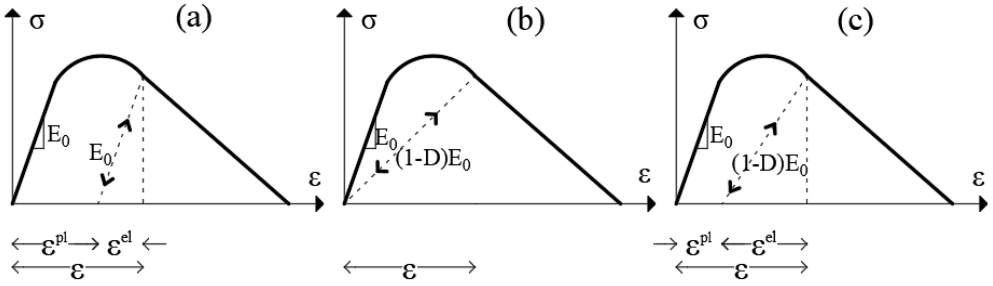

Figure 3. CDP model representation: (a) plasticity-only, (b) damage-only, (c) coupled damage–plasticity behavior

The stress–strain behavior under uniaxial loading in Figure 3 (c), representing the coupled damage–plasticity response, can be described by the following expressions:

$$\sigma_c = (1 - D_c)E_o(\varepsilon_c - \varepsilon_c^{pl}) \quad (1)$$

$$\sigma_t = (1 - D_t)E_o(\varepsilon_t - \varepsilon_t^{pl}) \quad (2)$$

where the subscripts t and c refer to tension and compression, respectively.

The compressive stress–strain curve used in the CDP model (Figure 4) begins with an initial linear segment defined as:

$$\sigma_{c1} = E_o\varepsilon_c \quad (3)$$

up to

$$\sigma_{c0} = 0.4f_{cm} \quad (4)$$

with

$$f_{cm} = f_{ck} + 8 \quad (5)$$

$$E_o = (0.8 + 0.2f_{cm}/88)E_{ci} \quad (6)$$

$$E_{ci} = 10000{f_{cm}}^{1/3} \quad (7)$$

The second segment of the curve, extending from $0.4f_{cm}$ to the peak compressive strength f_{cm}, follows a parabolic relationship as proposed in CEB-FIP (2010) [35]:

$$\sigma_{c2} = \frac{E_{ci}\frac{\varepsilon_c}{f_{cm}} - \left(\frac{\varepsilon_c}{\varepsilon_{cm}}\right)^2}{1 + \left(E_{ci}\frac{\varepsilon_{cm}}{f_{cm}} - 2\right)\frac{\varepsilon_c}{\varepsilon_{cm}}} f_{cm} \quad (8)$$

where the strain at peak compressive stress is:

$$\varepsilon_{cm} = 0.0022 \quad (9)$$

The post-peak descending branch is described by:

$$\sigma_{c3} = \left(\frac{2 + \gamma f_{cm}\varepsilon_{cm}}{2f_{cm}} - \gamma\varepsilon_c + \frac{\varepsilon_c^2\gamma}{2\varepsilon_{cm}}\right)^{-1} \quad (10)$$

$$\gamma = \frac{\pi^2 f_{cm}\varepsilon_{cm}}{2\left[\frac{G_{ch}}{l_{eq}} - 0.5f_{cm}\left(\varepsilon_{cm}(1-b) + b\frac{f_{cm}}{E_0}\right)\right]^2} \quad (11)$$

where l_{eq} denotes the characteristic length, and the crushing energy per unit area is given by:

$$G_{ch} = (f_{cm}/f_{tm})^2 G_F \quad (12)$$

$$G_F = 0.073{f_{cm}}^{0.18} \quad (13)$$

The parameter b is typically assumed to be 0.9.

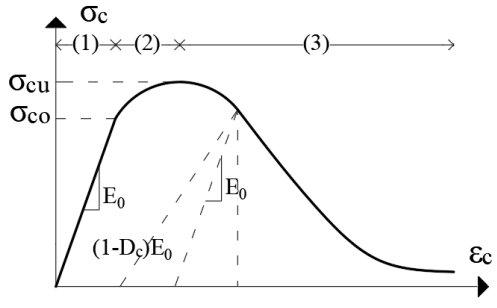

Figure 4. Definition of compressive behavior in terms of inelastic strain

The tensile stress degradation as a function of crack width W can be described using the expression proposed by Hordijk [36]:

$$\frac{\sigma_t(W)}{f_{tm}} = \left[1 + \left(C_1\frac{W}{W_C}\right)^3\right]e^{-C_2\frac{W}{W_C}} - \frac{W}{W_C}(1 + C_1^3)e^{-C_2} \quad (14)$$

where $\sigma_t(W)$ is the tensile stress corresponding to crack width W, and $\sigma_{to} = f_{tm}$ is the maximum tensile stress. Coefficients used are $C_1 = 3, C_2 = 6.93$, and the critical crack width is calculated as:

$$W_C = 5.14G_F/f_{tm} \quad (15)$$

The tensile strain from the stress–strain relationship (see Figure 5) is then determined using:

$$\varepsilon_t = \varepsilon_{tm} + W/l_{eq} \quad (16)$$

Within Abaqus, uniaxial stress–inelastic strain data is internally converted into stress–plastic strain format required by the software's numerical engine.

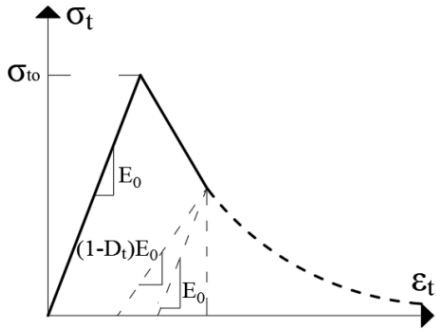

Figure 5. Definition of cracking strain in the tensile regime

4 Results and discussion

4.1 Model calibration

In order to calibrate the adopted modeling approach, the numerically obtained behavior of the slab under load—leading to failure—was compared with experimentally measured values [19]. For calibration purposes, the centrally loaded slab specimen S1, supported by a square-section column, was selected.

During the finite element modeling of the specimens, the geometry of the slab and column, as well as the reinforcement layout, were modeled to precisely match the actual test setup. The slab was loaded via the column, while load eccentricity, where applicable, was introduced by applying the force through a short rigid element placed at the bottom of the column. The load was applied as a concentrated force, as illustrated in Figure 6. This figure also shows the slab geometry, support conditions, and reinforcement layout for specimen S1.

Model calibration was conducted by varying selected parameters defining the CDP model, as well as by performing a mesh convergence study through increasing the number of finite elements in the model. Within the finite element method (FEM), convergence is assessed based on the mesh quality and the sensitivity of the results. Meshes may differ in terms of element size and their spatial arrangement.

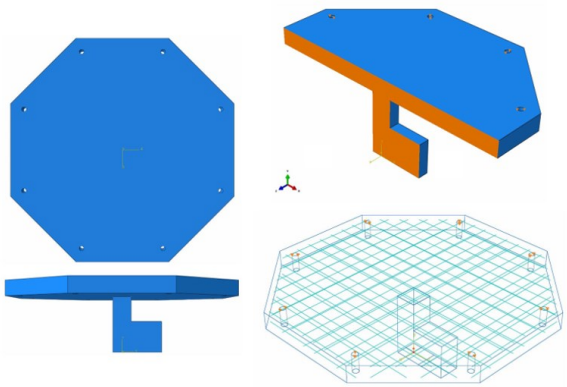

Figure 6. Geometry and support conditions of slab model S1

By increasing the number of finite elements, the degree of approximation is reduced, thus improving the accuracy of the numerical solution. Accordingly, convergence is evaluated by generating a sequence of successively refined meshes, where the size of elements is proportionally reduced, and the total number of elements is increased. With at least three consecutive meshes of different densities, it becomes possible to determine the trend of the numerical results toward the real (physical) value.

According to a study on the nonlinear analysis of punching shear in concrete slabs [37], it is recommended to use a mesh with element sizes ranging from 15 mm to 24 mm, with 24 mm representing the upper limit to avoid numerical hourglassing effects. To mitigate numerical issues, it is recommended to ensure that the slab thickness is divided into at least four elements.

In this study, mesh convergence was assessed using three different element sizes:

- 24 mm,
- 20 mm, and
- 15 mm.

A mesh size of 15 mm ensured 8 elements through the slab depth, while 20 mm and 24 mm meshes yielded 6 and 5 elements, respectively. The 24 mm mesh was considered the lower limit, as less than 5 elements through the slab thickness may cause C3D8R element distortion, leading to unreliable results.

The outcomes of this convergence study are shown in Table 3, where the punching load was taken as the force at which the slab experienced a significant increase in deflection under nearly constant load. This point corresponds to the transition in the load–deflection curve to an almost horizontal branch, indicating pronounced plastic deformations before failure due to punching.

Although the constitutive stress–strain law in tension is related to the finite element size, the results have shown that the element size still significantly influences the numerical outcomes. The dependency on the number of finite elements in the mesh is particularly reflected in the magnitude of deflection at the ultimate load (Figure 7).

The mesh with a 24 mm element size was found to be too coarse, producing an unrealistic and overly ductile representation of the slab behavior. On the other hand, the 15 mm element size was considered too fine, as its dimensions are comparable to the maximum aggregate size in the concrete, and thus not suitable for accurate modeling.

The results of the numerical simulation indicated that the adopted model with a 20 mm finite element size provides a precise prediction of the deflection at the ultimate load. However, the overall load–deflection response significantly deviates from the experimental curve in other loading phases. Specifically, the numerical model exhibits a considerably longer linear portion of the load–deflection curve than what was observed experimentally. According to the finite element analysis, the transition point—where the curve slope begins to change rapidly—occurs at approximately 150 kN, which is nearly twice the value observed in the experimental curve.

For this reason, the variation of the tensile strength values was chosen to systematically investigate the sensitivity of the load–deflection response to reductions in concrete tensile strength. The selected values approximately 2/3 and 1/3 of the initially determined tensile strength (3.09 MPa) allow assessment of how decreasing tensile capacity affects the slope of the curve and the onset of nonlinear behavior. This approach helps identify the range in which the numerical model can better reproduce the experimentally observed transition point and overall structural response. The corresponding results of the numerical analysis, showing the deflection response under increasing load, are presented in Figure 8.

Table 3. Mesh convergence – effect of finite element size on the estimated punching capacity

	Finite element size [mm]			Experimental results
	15	20	24	
Ultimate deflection [mm]	10.22	14.35	112.90	14.27
Ultimate load [kN]	230.03	252.69	275.35	246.99

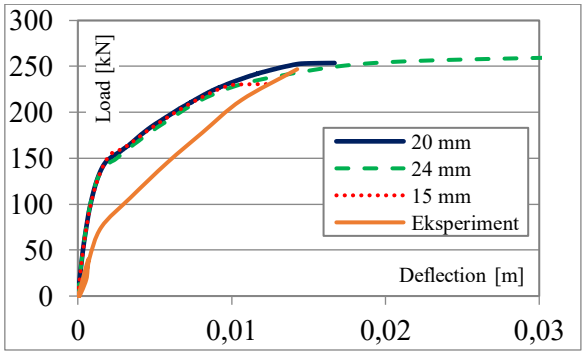

Figure 7. Load–deflection relationship depending on the finite element size

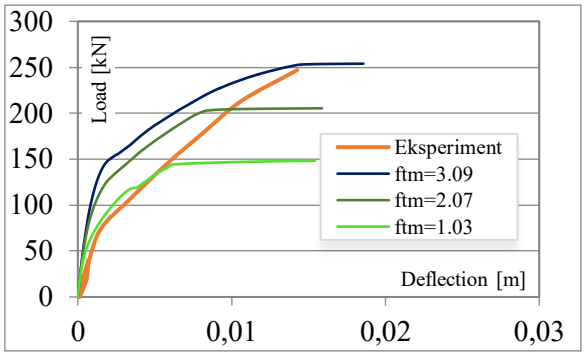

Figure 8. Load–deflection relationship depending on concrete tensile strength

The analysis results confirmed that a decrease in the maximum tensile strength of concrete leads to a reduction in the load intensity at which the slope of the load-deflection curve changes. In other words, cracks appear in the slab at lower load levels, which is expected since the punching shear capacity of an unreinforced slab depends on the tensile strength of the concrete.

The reduction in tensile strength also affected the failure load, resulting in a significant difference between the numerical and actual load values causing the slab failure. An increase in the slope of the curve after crack initiation can be achieved by adjusting the dilatancy angle ψ. The dilation angle (ψ) defines the direction of the plastic strain increment vector. In the CDP model, based on a non-associated flow rule, this vector is normal to the plastic potential function. According to Abaqus [30], the default eccentricity value of 0.1 assumes a nearly constant dilation angle over a wide range of confining pressures, while higher eccentricity values lead to a more curved potential function and a faster increase of the dilation angle as confining pressure decreases. The dilation angle ranges from 10° to 50°, with values between 30° and 50° used when modeling concrete with more pronounced plastic deformability, as higher angles lead to a more ductile response.

Numerical analyses were performed for ψ values of 30°, 38°, and 40°, with a maximum tensile strength $f_{tm} = 2.07\,MPa$ (Figure 9-right). For $f_{tm} = 1.03\,MPa$, three different dilatancy angles were analyzed: $\psi = 40°, \psi = 46°$, and $\psi = 48°$ (Figure 9-left).

From the diagram, it is observed that achieving the experimental failure load in the model with tensile strength $f_{tm} = 2.07\,MPa$ requires a dilatancy angle of $\psi = 38°$ or higher. For the model with tensile strength $f_{tm} = 1.03\,MPa$, a significantly larger dilatancy angle of $\psi = 46°$ is required. This curve provides the closest numerical response to the actual slab behavior under loading. However, when observing the crack pattern on the tensile surface of the slab, at $\psi = 46°$, cracks are mostly concentrated above the column (Figure 10), which differs from the experimental results where cracks initially appeared above the column corners and gradually extended towards the slab edges.

Figure 10-left shows cracks resulting from a load of approximately 70 kN, i.e., at the load intensity where the load-deflection curve changes its slope. At this load, only surface cracks appear in the concrete cover layer, which can be seen in the slab cross-section. Increasing the load to about 100 kN causes the appearance of an inclined crack in the slab cross-section, which further widens with increasing load and eventually forms the punching cone due to failure, as shown in Figure 10-right. The same figure (Figure 10-right) presents the crack pattern at the failure load of approximately 240 kN.

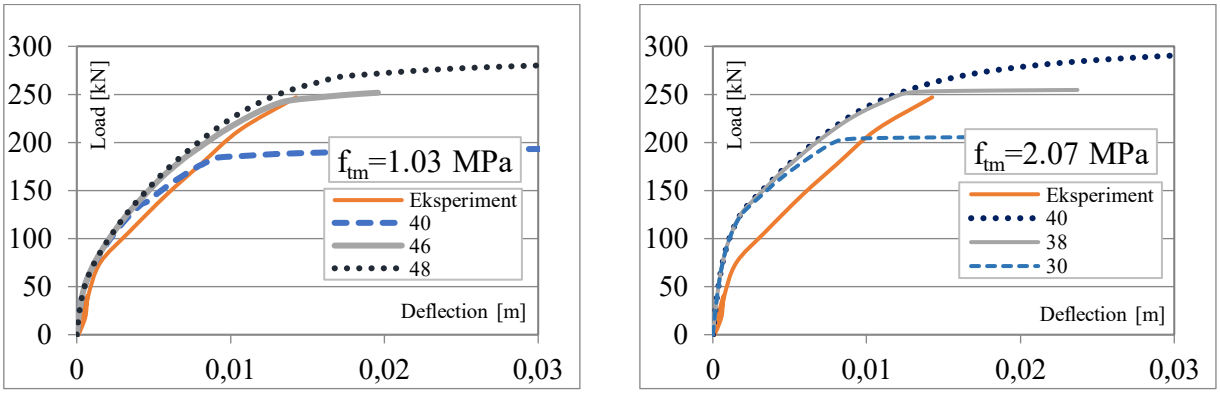

Figure 9. Load–deflection relationship depending on the variation of the dilation angle

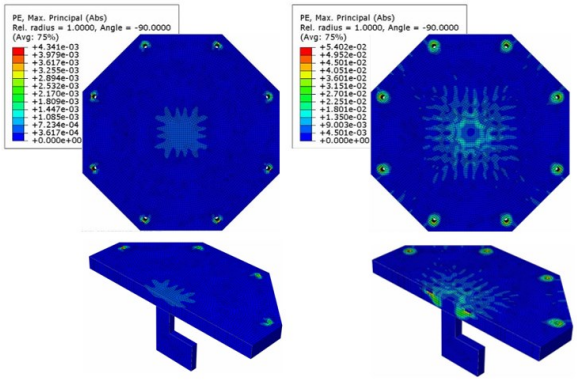

Figure 10. Cracking pattern in the slab for a dilatancy angle of $\psi = 46°$ *and* $f_{tm} = 1.03\ MPa$

By reducing the dilatancy angle ψ (Figure 11), a more accurate crack distribution on the tensile surface of the slab is obtained. At the initial loading stage, cracks appear above the support corners, and at higher loads, cracks intensify above the support, forming the punching cone due to failure.

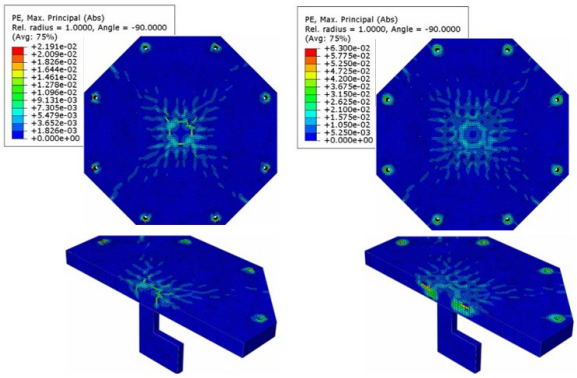

Figure 11. Cracking pattern in the slab for dilatancy angle $\psi = 38°$ *and* $f_{tm} = 2.07\ MPa$

For this reason, in order to numerically reproduce both the experimentally obtained failure load and deflection, while also aiming to realistically capture the crack distribution, the lowest recommended value of the parameter $\alpha_{ct,sp} = 0.67$ [31] was adopted in the expression for defining the tensile strength of concrete $f_t = \alpha_{ct,sp} \cdot f_{ct,sp}$. Accordingly, a tensile strength of $f_t = 2.30\ MPa$ was used in the subsequent analyses.

The critical dilatation is largely dependent on the fracture energy G_f, which according to the CEB-FIP Model Code 2010 [35] is calculated as:

$$G_f = 0.073 f_{cm}{}^{0.18} = 0.141 N/mm$$

If the fracture energy is calculated according to the CEB-FIP Model Code 1990 [38], the critical dilatation will have a lower value, and the descending branch of the stress-dilatation diagram will show a steeper drop:

$$G_F = G_{fo}(f_{cm}/f_{cmo})^{0.7} = 0.0774 N/mm$$

where:

$f_{cmo} = 10MPa$

$G_{fo} = 0.030\ N/mm$ for $d_{max} = 16mm$

The dependence of the slab's load- deflection response on the variation of fracture energy values is shown in Figure 12. In the numerical analysis, the tensile strength of concrete was taken as $f_t = 2.30$ MPa, and the dilatancy angle as $\psi = 38°$. The analysis results indicated that choosing the lower fracture energy value ($G_F = 0.0774 N/mm$) provides a numerical response closer to the real, experimentally determined slab behavior. Therefore, for all subsequent slab simulations, a dilatancy angle of $\psi = 38°$ will be adopted, along with the fracture energy expression: $G_F = G_{fo}(f_{cm}/f_{cmo})^{0.7}$.

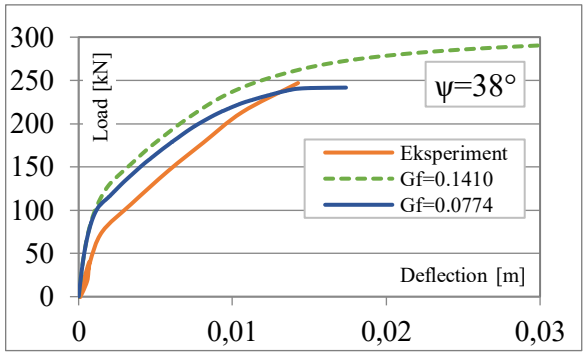

Figure 12. Load-deflection relationship depending on the variation of fracture energy

Model calibration was also performed with respect to the variation of the viscosity parameter μ. It is known that the viscosity parameter influences the convergence rate of the model during the material softening phase. To avoid distortion of the results, the value of this parameter should be approximately 15% of the selected time increment size in Abaqus [30]. Due to the high nonlinearity in the analysis of punching shear in RC slabs, the time increment cannot be fixed and is therefore set automatically. For this reason, the influence of the viscosity parameter on the numerical analysis results will be examined for three different values: μ=0.000001, μ=0.00001 i μ=0.0001.

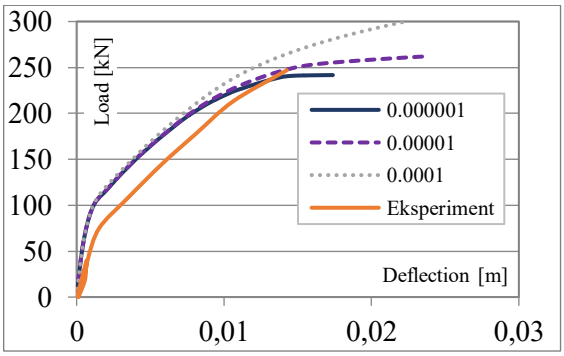

Figure 13. Load- deflection relationship depending on the viscosity parameter μ

The numerical analysis results (Figure 13) showed that the viscosity parameter value of μ=0.000001 best corresponds to the experimentally measured results, and therefore this value will be adopted in all subsequent analyses.

After confirming that the numerically obtained results corresponded well to the experimental data, the same model was applied to all other experimentally tested slabs. The parameters defining the CDP model in Abaqus were adopted as follows: $Kc = 2/3, \psi = 38°, \sigma_{bo}/\sigma_{co} = 1.16, e = 0.1, \mu = 0.000001$. A finite element size of 20 mm was adopted. The

maximum tensile strength of concrete was determined as $f_t = 0.67 \cdot f_{ct,sp}$ [31], while the fracture energy was calculated according to the CEB-FIP Model Code 90 [38] as $G_F = G_{fo}(f_{cm}/f_{cmo})^{0.7}$.

4.2 Load–deflection response and cracking pattern

Following the conducted analysis and calibration of the CDP model on slab S1, the adopted model was applied to estimate the punching shear force, deflection, and crack patterns under loading for all experimentally tested concrete specimens. Slab S1, being the simplest among the seven analyzed slabs, was used for model validation and assessment of its reliability before being applied to more complex configurations.

Figure 14 presents a comparison of the load–deflection response for slab S1, obtained using the FEM and experimental testing (Exp). During experimental testing, punching failure occurred under a load of 246.99 kN, with a maximum deflection above the column of 14.27 mm. The numerical results show good agreement with the experimental data in terms of both the ultimate load and the corresponding deflection. The observed deviations are within 3%, which confirms the validity of the model. A minor discrepancy was noted in the linear portion of the response, where nonlinear behavior begins at approximately 100 kN in the FEM analysis, while the experimental data indicates the onset of nonlinearity around 75 kN.

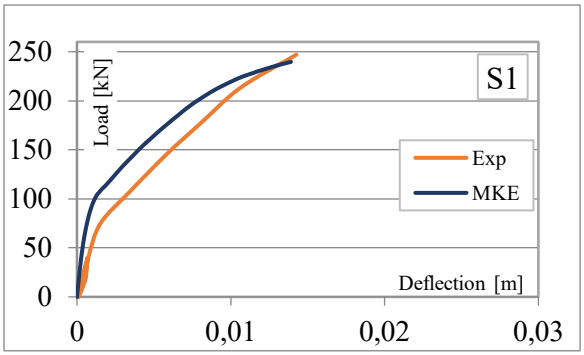

Figure 14. Load–deflection response of slab S1

Figure 15-left shows the crack propagation in the numerical model at the ultimate load, with a clearly formed punching cone through the slab thickness. Figure 15-right shows a photograph of the experimental specimen after failure. In both cases, cracks are concentrated above the loaded area, and the crack distribution demonstrates a high degree of correlation between the numerical and experimental results.

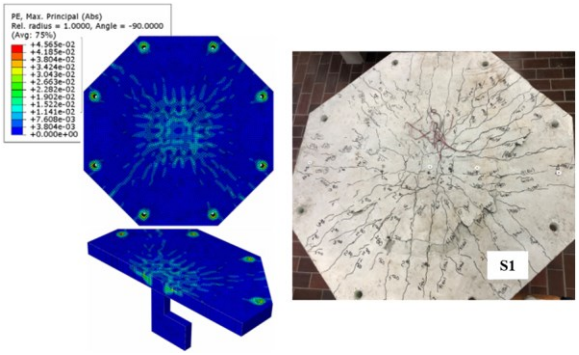

Figure 15. Cracking pattern at failure in RC slab S1

The modeling of eccentrically loaded slab S2 without an opening was carried out using the same methodology as for slab S1. Based on the numerical results, a comparison was made with experimental data to verify the model's accuracy. The diagram in Figure 16 shows the relationship between applied load and maximum deflection, indicating good agreement up to the failure load. The experimental punching load was 187.28 kN, while the numerical result was 194.52 kN. The maximum deflection obtained using FEM was 12.82 mm, compared to 10.22 mm measured experimentally.

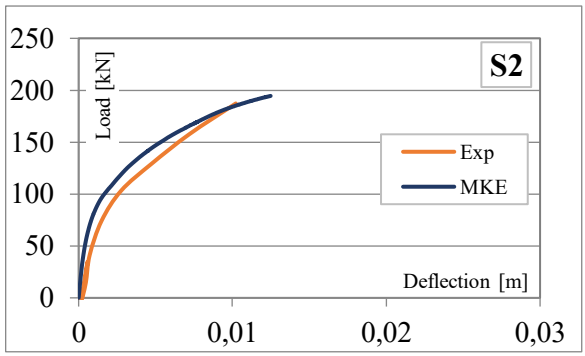

Figure 16. Load–deflection response of slab S2

Crack propagation is presented in Figure 17. Both the numerical model and the experimental photo exhibit very good agreement. Cracks predominantly developed above the loaded zone and follow the direction of the eccentric load. As expected, an inclined shear crack appears only in the region influenced by the eccentric force.

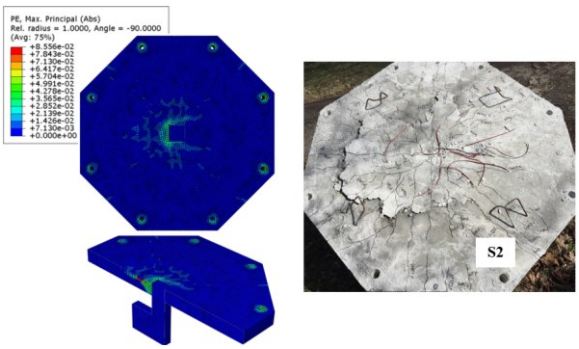

Figure 17. Cracking pattern at failure in RC slab S2

Slab S3 was centrally loaded and included a square opening adjacent to the column face. The purpose of the analysis was to numerically confirm the influence of the opening on punching shear capacity. The load–deflection comparison shown in Figure 18 presents both numerical (punching load: 166.32 kN, deflection: 10.68 mm) and experimental (183.36 kN, deflection: 10.75 mm) results. The two curves match up to approximately 60 kN, after which the experimental curve changes slope, while the numerical model maintains linear behavior until around 90 kN. The deviation in ultimate load is about 9%, while the deflection is practically identical.

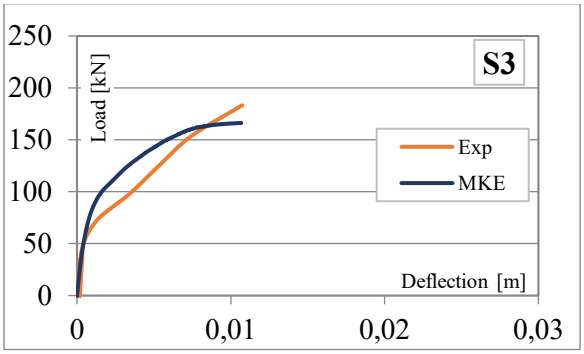

Figure 18. Load–deflection response of slab S3

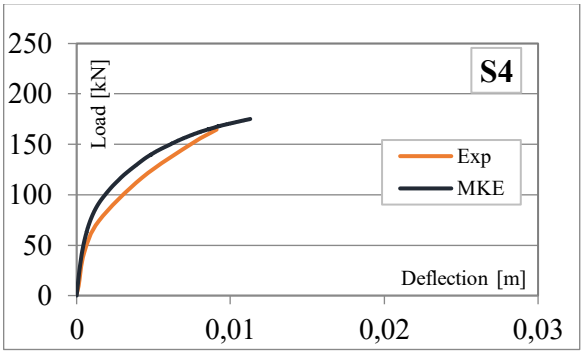

Figure 20. Load–deflection response of slab S4

The crack pattern in the numerical model at the load level where the numerical analysis ceased to converge is compared in Figure 19 with the actual crack distribution observed after punching failure occurred. The punching cone is shown through both longitudinal and transverse sections of the slab. In this case as well, the propagation of numerically predicted cracks at the ultimate load shows good agreement with the actual crack pattern observed in the centrally loaded slab with an opening adjacent to the face of a square column.

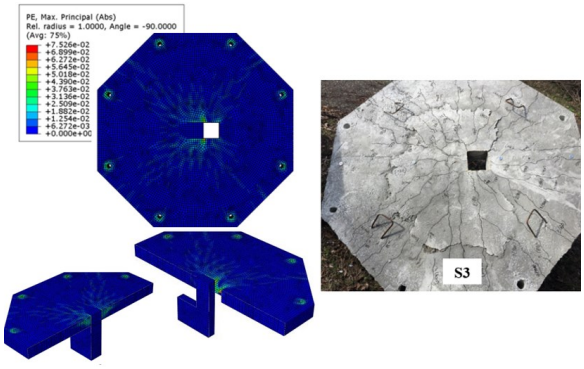

Figure 19. Cracking pattern at failure in RC slab S3

The results for slab S4, with an opening located on the side opposite to the direction of eccentric loading, are presented in Figure 20. A good level of agreement was observed in the linear phase of the load–deflection behavior. The numerical model predicts a slightly higher punching load (175.13 kN) and deflection (11.29 mm) compared to the experimental results (punching load: 164.81 kN, deflection: 9.10 mm).

Crack propagation is shown in Figure 21. Both the numerical and experimental models demonstrate crack concentration above the loaded area, with a clearly visible inclined crack on the side of the applied force, which confirms the correctly identified eccentric behavior.

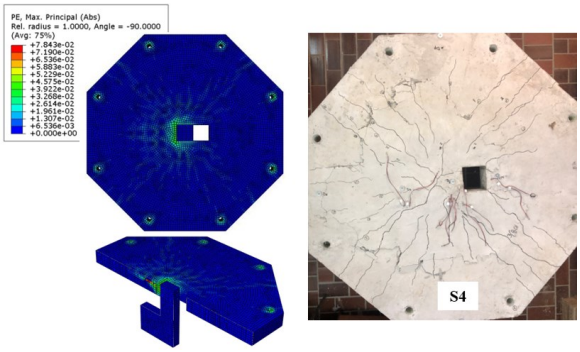

Figure 21. Cracking pattern at failure in RC slab S4

For slab S5, which includes an opening adjacent to the column face on the same side as the applied eccentric load, the initial numerical analysis was performed following the same principles as for the previous slabs. However, the results showed that modeling the slab with this setup (FEM-Gf = 0.077) significantly underestimates the punching shear capacity, while the deflection remains approximately equal to that recorded in the experimental test. For this reason, a new numerical analysis was carried out using a fracture energy value of $G_f = 0.141 N/mm$. This resulted in a higher tensile strain capacity and a softer descending branch in the tensile stress–strain diagram. The response of the slab under load with the modified material properties is shown in the diagram labeled FEM-Gf = 0.141. This adjustment yielded a punching load and ultimate deflection that closely matched the experimental results (Table 4).

Table 4. Ultimate load and deflection for slab S5

	FEM-Gf=0.077	FEM-Gf=0.141	Exp	Exp/ FEM-Gf=0.077	Exp/ FEM-Gf=0.141
Ultimate deflection [mm]	6.68	6.98	6.44	0.96	0.92
Ultimate load [kN]	119.59	137.75	139.78	1.17	1.01

The load–deflection diagram (Figure 22) describing the behavior of the slab under loading shows good agreement up to a load of approximately 60 kN, after which the experimental curve changes its slope, marking the end of the slab's linear response. According to the FEM analysis, linear behavior persists up to approximately 80 kN, which results in minor discrepancies in the nonlinear portion of the slab's response.

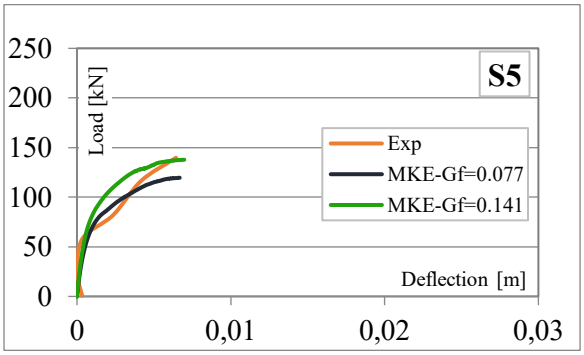

Figure 22. Load–deflection response of slab S5

The crack pattern in the numerical model at the load level where the analysis ceased to converge is compared with the actual crack distribution observed after punching failure occurred (Figure 23). The crack propagation at ultimate load according to the FEM model shows good agreement with the real crack pattern caused by punching in the eccentrically loaded slab with an opening adjacent to the column face. Both the numerical and experimental models reveal that, despite the eccentric loading, cracks are concentrated in the area directly above the column. This occurred due to the presence of the opening adjacent to the column face on the side of the slab where the eccentric load is applied.

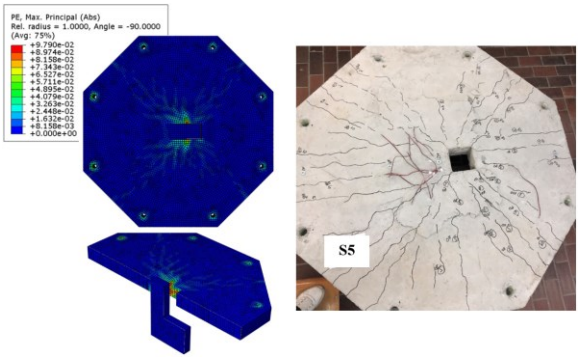

Figure 23. Cracking pattern at failure in RC slab S5

The results of the numerical analysis for slab S6 are presented alongside the experimental results (punching load: 218.62 kN, deflection: 7.11 mm), with the numerical model yielding a punching load of 226.59 kN and a deflection of 11.21 mm. Although the FEM analysis indicates a slightly greater deflection at the ultimate load, the overall behavior of the slab in both numerical and experimental models is relatively consistent across all loading phases (Figure 24).

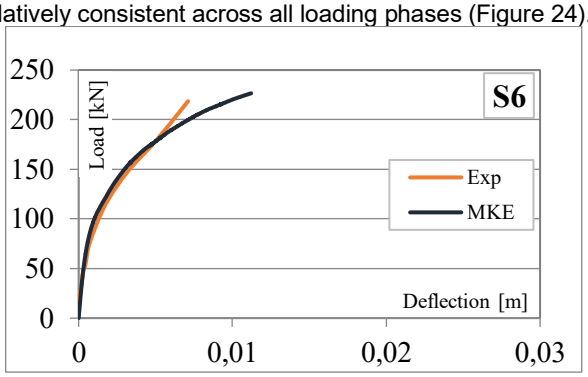

Figure 24. Load–deflection response of slab S6

The change in slope of the load–deflection curve indicates the load at which the slab transitions to nonlinear behavior, i.e., the point at which cracks begin to form in the RC specimen. For both the numerical and experimental models, the linear behavior ends at approximately 100 kN. As the load increases, cracks begin to propagate, mostly in the area subjected to eccentric loading. As with previous slabs, the inclined crack appears only on the side of the slab where the eccentric force is applied. Figure 25 shows a comparison of crack patterns at the ultimate load in both the numerical and experimental models, demonstrating very good correlation.

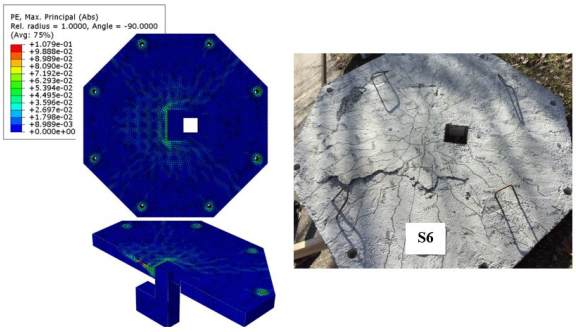

Figure 25. Cracking pattern at failure in RC slab S6

As with slab S5, slab S7 was also modeled using two different descriptions of concrete tensile behavior. The S7 slab differs from S5 only in the shape and dimensions of the column. Slab S7 is supported by a rectangular column with dimensions 15×30 cm and includes a square opening adjacent to the column face. The opening is located on the side of the slab where the eccentric load is applied. The numerical analysis was carried out for two values of fracture energy: $G_f = 0.141 N/mm$ and $G_f = 0.077 N/mm$. The results showed that using the lower fracture energy (FEM-Gf=0.077, see Figure 26) significantly underestimates the punching shear capacity. When using the higher fracture energy ($G_f = 0.141 N/mm$) a higher ultimate load was obtained, with only an 8% deviation from the experimental result (Table 5).

Table 5. Ultimate load and deflection for slab S7

	FEM-Gf=0.077	FEM - Gf=0.141	Exp	Exp/ FEM - Gf=0.077	Exp/ FEM - Gf=0.141
Ultimate deflection [mm]	7.72	8.59	8.26	1.07	0.96
Ultimate load [kN]	154.10	172.98	187.68	1.22	1.08

The load–deflection curves show good agreement up to a load of approximately 140 kN, after which the FEM-Gf=0.077 curve exhibits a steep increase in deflection with minimal additional loading, ultimately leading to analysis failure. The FEM-Gf=0.141 curve closely follows the experimental curve up to a load of about 160 kN, after which small deviations appear, with the numerical curve slightly underestimating the ultimate punching capacity.

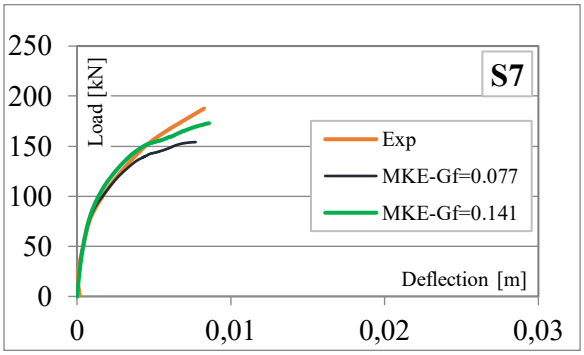

Figure 26. Load–deflection response of slab S7

The crack pattern in the numerical model at the load level where the analysis stopped converging is compared with the actual crack pattern after punching failure occurred (Figure 27). The distribution of cracks at the ultimate load according to FEM analysis is in very good agreement with the actual crack distribution caused by punching failure in the eccentrically loaded slab with an opening adjacent to the column face. As observed with slab S5, both the numerical and experimental models show that, despite the eccentric load, cracks are concentrated in the area directly above the column. This behavior is attributed to the presence of the opening located adjacent to the column face on the same side where the eccentric force is applied.

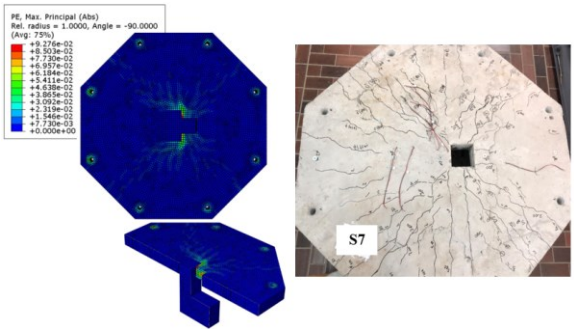

Figure 27. Cracking pattern at failure in RC slab S7

4.3 Review of obtained results

The punching shear process was analyzed using the CDP model, which was previously calibrated based on specimen S1. Calibration was performed by varying relevant CDP model parameters and the finite element mesh size. Among the three considered mesh sizes, elements of 20 mm provided the most accurate estimates of the critical deformation caused by the ultimate load. The obtained results demonstrated that this approach provides satisfactory accuracy, indicating that it is not strictly necessary to perform mesh calibration for each model individually. However, it would be valuable in future research to verify the mesh calibration on additional slabs in order to further confirm the model's reliability and general applicability.

To achieve a realistic linear response aligned with experimental data, three different concrete tensile behavior diagrams were investigated. The analysis showed that reducing the maximum tensile strength of concrete decreases the load level at which the slope of the load–deflection curve changes. In other words, cracks form at lower loads, as expected, since the punching shear capacity of a slab depends on the concrete tensile strength. For this reason, the lowest recommended value of the parameter $\alpha_{ct,sp} = 0.67$ [31] was adopted in the expression for defining the tensile strength of concrete $f_t = \alpha_{ct,sp} \cdot f_{ct,sp}$.

Based on this tensile strength and the corresponding tensile behavior diagram, the influence of the dilation angle ψ was analyzed. The criterion for selecting the optimal value was obtaining a punching load and corresponding deflection as close as possible to the experimental results, along with a visually similar crack distribution. A dilation angle of $\psi = 38°$ proved to be the most adequate and was adopted for further analysis.

The model calibration also included analysis of the viscosity parameter μ, which affects convergence during the material softening phase. It is recommended that this parameter be around 15% of the chosen time increment in Abaqus [30]. Given the high nonlinearity of the problem and the automatic determination of time increments, the optimal value of μ was determined by testing three different values. The most reliable results were obtained for $\mu = 0.000001$.
In addition, the influence of fracture energy on the numerical results was analyzed. Fracture energy G_f is not entirely size-independent in concrete and varies across different regions of a specimen. Boundary conditions and specimen geometry strongly affect the G_f, as the proximity of edges or free surfaces can constrain the development of the fracture process zone [39]. These variations in fracture energy are reflected in the observed crack propagation patterns, which allow the analyzed slabs to be broadly classified into two groups. The first group (centrally and eccentrically loaded slabs S1, S2, S3, S4, S6) is characterized by cracks that develop freely across the slab, with the highest concentration occurring in the region subjected to the applied load. The second group (eccentrically loaded slabs S5 and S7) exhibits cracks concentrated directly above the columns, due to the presence of openings in the load application region.

Two expressions were used for calculating fracture energy:

- CEB-FIP Model Code 2010 [35]: $G_f = 0.073 {f_{cm}}^{0.18}$.

This approach proved more suitable for modeling eccentrically loaded slabs S5 and S7.

- CEB-FIP Model Code 90 [38]: $G_F = G_{fo}(f_{cm}/f_{cmo})^{0.7}$

This formula provided better agreement for slabs S1, S2, S3, S4, and S6.

Once it was confirmed that the calibrated model accurately reproduces the experimental results for specimen S1, the same model was applied to all other analyzed slabs. A comparative overview of the numerical and experimental values of punching load and the corresponding deflection is presented in Table 6.

Table 6. Comparison of experimental and numerical results

Slab	Ultimate load [kN]		Exp/ FEM	Ultimate deflection [mm]		Exp/ FEM
	FEM	Exp		FEM	Exp	
S1	240.10	246.99	1.03	14.09	14.27	1.01
S2	194.52	187.28	0.96	12.83	10.22	0.82
S3	166.32	183.36	1.10	10.68	10.75	1.01
S4	175.13	164.61	0.94	11.29	9.10	0.81
S5	137.75	139.78	1.01	6.98	6.44	0.92
S6	226.59	218.62	0.96	11.21	7.11	0.63
S7	172.98	187.68	1.08	8.59	8.26	0.96

It was observed that discrepancies in the calculated punching load do not exceed 10%, indicating satisfactory agreement. For slabs with central loading (S1 and S3), the numerically obtained deflection were almost identical to the experimentally measured ones, with a deviation of only 1%. Larger deviations, up to 20%, were recorded for eccentrically loaded slabs, except for S6. Although the numerical model for S6 predicted a higher deflection, the slab behavior during all other loading phases showed good agreement with experimental findings.

Based on the conducted analysis, it can be concluded that applying the CDP model with carefully defined parameters enables reliable estimation of the punching load in various types of RC slabs. This approach allows for efficient investigation of the influence of different factors on punching shear capacity without the need for complex and costly experimental testing, thereby saving significant time and resources.

5 Conclusions

This study aimed to provide a detailed analysis of the key parameters required for the reliable definition of the CDP model within nonlinear numerical simulations of punching shear in flat slabs. These values provide a balanced representation of concrete's inelastic behavior under multiaxial stress states, making the CDP model suitable for simulating punching shear phenomena in RC slabs. After completing the calibration of the model on the reference slab S1, the same numerical model was applied to six additional slabs, which differed in three main aspects: the presence of openings in the slab, the eccentricity of loading, and the geometry (cross-sectional dimensions) of the supporting column. Based on the obtained numerical results, the following conclusions can be drawn:

- After successful calibration on one representative specimen, the CDP model proved reliable in accurately predicting the behavior of different RC slab types.
- A mesh convergence study was conducted to determine the optimal finite element size for reliable punching shear analysis. Results showed that element size significantly influences numerical accuracy, particularly the deflection at ultimate load. The 24 mm mesh was too coarse, leading to unrealistic ductility, while the 15 mm mesh was overly fine and not physically appropriate. A 20 mm mesh provided the best balance between accuracy and computational efficiency and was adopted for further simulations.
- To achieve accurate numerical correlation with the experimental failure load and deflection, a tensile strength of $f_t = 0.67 \cdot f_{ct,sp}$ and a dilatancy angle of $\psi = 38°$ were identified as optimal. While higher dilatancy angles improve load prediction for lower tensile strengths, they produce unrealistic crack patterns. Therefore, the chosen parameters best replicate both structural response and cracking behavior and are adopted for further analysis.
- The viscosity parameter μ = 0.000001 gave the most stable and reliable convergence behavior in the softening phase of the material response.
- The analysis indicates that fracture energy G_f in concrete is not uniform and is influenced by specimen geometry and boundary conditions, which affect crack propagation patterns. Consequently, different expressions for G_f are better suited for different slab types: The Model Code 2010 [35] approach was more suitable for eccentrically loaded slabs with an opening on the load application side (S5 and S7), while the Model Code 90 [38] formula gave better accuracy for all other analyzed slabs (S1, S2, S3, S4, and S6).
- The difference between numerical and experimental punching loads did not exceed 10%, confirming the model's accuracy.
- For centrally loaded slabs, numerical and experimental deflections were nearly identical (within 1%), while eccentrically loaded slabs showed slightly larger deviations, up to 20%.
- Applying the CDP model with carefully defined parameters enables a reliable estimation of punching shear capacity, significantly reducing the need for expensive and time-consuming experimental tests.

CRediT authorship contribution statement

According to the Contributor Role Taxonomy (CRediT) guidelines, the authors contributed to this work as follows:

Smilja Bursać: Writing – Original Draft Preparation; Conceptualization; Methodology; Formal Analysis; Software; Validation; Visualization.

Martina Vojnić Purčar: Review & Editing; Methodology.

Ljiljana Kozarić: Review & Editing; Methodology.

Mila Svilar: Review & Editing; Methodology.

Declaration of competing interest

The authors declare that they have no known competing financial interests or personal relationships that could have appeared to influence the work reported in this paper.

Acknowledgments

The present work has been supported by The Provincial Secretariat for Higher Education and Scientific Research, Autonomous Province of Vojvodina, Republic of Serbia (Project No. 142-451-2640/2021-01).

References

[1] A.N. Talbot, Tests of reinforced concrete slabs: resistance to punching and shearing, University of Illinois Engineering Experiment Station, 1913.

[2] S. Kinnunen, H. Nylander, Punching of concrete slabs without shear reinforcement, Transactions of the Royal Institute of Technology, Stockholm, 1960. doi: 10.1007/s12205-018-1505-5.

[3] J. Moe, Shearing strength of reinforced concrete slabs and footings under concentrated loads, Development Department Bulletin No. D47, Portland Cement Association, Skokie, USA, 1961.

[4] A. Muttoni, Punching shear strength of reinforced concrete slabs without transverse reinforcement, ACI Structural Journal, Vol. 105, No. 4, 2008, 440–450. doi: 10.14359/56428.

[5] S. Marinković, Granično stanje probijanja armiranobetonskih i prethodno napregnutih ploča, Građevinski kalendar, Vol. 39, 2006, 305-351.

[6] R.Z. Alrousan, B.R. Alnemrawi, The influence of concrete compressive strength on the punching shear capacity of reinforced concrete flat slabs under different opening configurations and loading conditions, Structures, 44, 2022, 101–119. https://doi.org/10.1016/j.istruc.2022.07.091.

[7] N. Shatarat, D. Salman, Investigation of punching shear behavior of flat slabs with different types and arrangements of shear reinforcement, Case Studies in Construction Materials, 16, 2022. https://doi.org/10.1016/j.cscm.2022.e01028.

[8] R. Zufarihsan, A. Tambusay, B. Suryanto, P. Suprobo, Predicting the punching failure of lightly reinforced concrete flat slabs without shear reinforcement, Structures, 74, 2025. https://doi.org/10.1016/j.istruc.2025.108473

[9] M.P. Ferreira, M.G. Costa, M.J.M. Pereira Filho, M. Fernández Ruiz, D.V. Faria, Influence of stirrup detailing on the punching resistance of reinforced concrete flat slabs, Engineering Structures, 336, 2025. https://ssrn.com/abstract=5095740 or http://dx.doi.org/10.2139/ssrn.5095740

[10] R. Awad, A. Al Ateyat, M.T. Junaid, Z. Al-Sadoon, S. Altoubat, M. Maalej, S. Barakat, Punching shear capacity of fiber-reinforced concrete suspended slabs: Database analysis and models assessments, Journal of Building Engineering, 83, 2024. https://doi.org/10.1016/j.jobe.2023.108433

[11] L. Lin, D. Liu, D. Zhang, X. Wu, Y. Zhang, C. Wu, H. Wang, Y. Lu, Punching shear strength of reinforced ultra-high performance concrete circular slabs with openings, Structures, 79, 2025. https://doi.org/10.1016/j.istruc.2025.109358

[12] A.D. Almutairi, M. Elsayed, M.M. Abdelaziz, H.A. Dahish, Punching shear capacity of rubberized high strength concrete slabs containing waste glass powder as cement substitute, Structures, 78, 2025. https://doi.org/10.1016/j.istruc.2025.109222

[13] A. Türer, Ö. Mercimek, Ö. Anıl, Y. Erbaş, Experimental and numerical investigation of punching behavior of two-way RC slab with different opening locations and sizes strengthened with CFRP strip, Structures, 49, 2023, 918–942. https://doi.org/10.1016/j.istruc.2023.01.157

[14] B.R. Alnemrawi, R.Z. Al-Rousan, A.N. Ababneh, The role of CFRP strengthening in improving the punching shear behavior of heat-damaged flat slabs with openings of different sizes and locations, Engineering Failure Analysis, 160, 2024. https://doi.org/10.1016/j.engfailanal.2024.108208

[15] H.M.F. Mostafa, A.A. Mahmoud, T.S. Mostafa, A.N.M Khater, Experimental and analytical punching shear behavior of reinforced concrete flat slabs having internal GFRP gratings, Structures, 60, 2024. https://doi.org/10.1016/j.istruc.2024.105882

[16] W. Mansour, W. Li, M. Ghalla, M. Badawi, M.A. El Zareef, Improving the punching capacity of two-way RC flat slabs via external strengthening using aluminum sheets, Construction and Building Materials, 420, 2024. https://doi.org/10.1016/j.conbuildmat.2024.135611

[17] S. Fayed, A. Basha, S.A. Yehia, Punching shear strength of concrete slabs resting on the ground reinforced with different forms of steel mesh fabric, Structures, 76, 2025. https://doi.org/10.1016/j.istruc.2025.109029

[18] S. Živković, M. Bešević, M. Vojnić Purčar, Lj. Kozarić, Nonlinear finite element analysis of punching shear strength of eccentrically loaded RC flat slabs with opening, KSCE J. Civ. Eng., Vol. 23, No.11, 2019, 4771–4780. https://doi.org/10.1007/s12205-019-0075-5

[19] S. Bursać, M. Bešević, M. Vojnić Purčar, Lj. Kozarić, N. Đurić, Experimental analysis of punching shear strength of eccentrically loaded slab with the opening along the face of the internal column, Eng. Struct, 249, 2021. https://doi.org/10.1016/j.engstruct.2021.113359.

[20] D. Vargas, E.O.L. Lantsoght, A.S. Genikomsou, Flat Slabs in Eccentric Punching Shear: Experimental Database and Code Analysis, Buildings, Vol. 12, 2022, 2092. https://doi.org/10.3390/buildings12122092

[21] J.A. Silva, M.G. Marques, M.L. Trautwein, R.B. Gomes, G.N. Guimaraes, Punching of reinforced concrete flat slabs with holes and shear reinforcement, REM, Int. Eng. J., Ouro Preto, Vol. 70, No 4, 2017, 407-413. doi: 10.1590/0370-44672017700022.

[22] A. Abdullah, C.G. Bailey, Z.J. Wu, Tests investigating the punching shear of a column–slab connection strengthened with non-prestressed or prestressed FRP plates, Constr Build Mater, Vol. 43, 2013, 1134–1144. https://doi.org/10.1016/j.conbuildmat.2013.07.012

[23] B. Adetifa, M.A. Polak, Retrofit of interior slab-column connections for punching using shear bolts, ACI Structural Journal, Vol. 102, No. 2, 2005, 268–274. doi: 10.14359/14278.

[24] H. Marzouk, A. Hussein, Experimental Investigation on the Behavior of High-Strength Concrete Slabs, ACI Structural Journal, Vol. 88, No. 6, 1991, 701-713.

[25] Z. Brujić, D. Kukaras, R. Folić, S. Ali, A. Čeh, Punching shear strength of eccentrically loaded RC flat slabs without transverse reinforcement, Građevinar, Vol. 70, No. 9, 2019, 757-770. doi: 10.14256/JCE.2404.2018.

[26] T. Urban, M. Gołdyn, J. Krakowski, Ł. Krawczyk, Experimental investigation on punching behavior of thick reinforced concrete slabs, Archives of Civil Engineering, LIX, 2, 2013. doi: 10.2478/ace-2013-0008

[27] R.Z. Alrousan, B.R. Alnemrawi, Punching shear behavior of FRP reinforced concrete slabs under different opening configurations and loading conditions, Case Studies in Construction Materials, Vol. 17, 2022. https://doi.org/10.1016/j.cscm.2022.e01508.

[28] R.Z. Alrousan, B.R. Alnemrawi, The influence of concrete compressive strength on the punching shear capacity of reinforced concrete flat slabs under different opening configurations and loading conditions, Structures, Vol. 44, 2022, 101-119. https://doi.org/10.1016/j.istruc.2022.07.091.
[29] M. Hallgren, S. Kinnunen, B. Nylander, Punching shear tests on column footings, Nordic Concrete Research, Stockholm, 1998.
[30] ABAQUS, 6.14, Dassault Systemes Simulia Corp. Provid. RI, USA, 2014.
[31] S. Marinsković, N. Pecić, Teorija betonskih konstrukcija, Akademska misao, Beograd, 2018.
[32] Eurocode 2. Design of concrete structures – Part 1-1: General rules and rules for buildings. SRPS EN 1992-1-1, 2015.
[33] J. Lee, G. L. Fenves, Plastic damage model for cyclic loading of concrete structures, ASCE Journal of Engineering Mechanics, Vol. 124, 1998, 892-900. doi:10.1061/(asce)0733-9399(1998)124:8 (892).
[34] S. Oller, Nonlinear dynamics, International Center for Numerical Methods in Engineering, Technical University of Catalonia, Spain, 2014.
[35] CEB-FIP, Model Code 2010, Thomas Telford, London, 2010.
[36] D. A. Hordijk, Tensile and tensile fatigue behavior of concrete; experiments, modeling and analyses, Heron, Vol. 37, No. 1, 1992, 3-79.
[37] A. Genikomsou, Nonlinear finite element analysis of punching shear of reinforced concrete slab-column connections, University of Waterloo, 2016.
[38] CEB-FIP, Model Code 1990, Comité Euro-International du Béton, 1993.
[39] D. Kai, H. Xiaozhi , F.H. Wittmann, Boundary effect on concrete fracture and non-constant fracture energy distribution, Engineering Fracture Mechanics, Vol. 70, No. 16, 2003, 2257-2268. https://doi.org/10.1016/S0013-7944(02)00223-0.